SANDIA REPORT

SAND2005-0860
Unlimited Release
Printed February 2005

Solution-Based Nanoengineering of Materials

Z. Ryan Tian, Louise Criscenti, Erik Spoerke, Bonnie McKenzie, Randy Cygan, Jun Liu, and James Voigt

Prepared by
Sandia National Laboratories
Albuquerque, New Mexico 87185 and Livermore, California 94550

Sandia is a multiprogram laboratory operated by Sandia Corporation,
a Lockheed Martin Company, for the United States Department of Energy's
National Nuclear Security Administration under Contract DE-AC04-94AL85000.

Issued by Sandia National Laboratories, operated for the United States Department of Energy by Sandia Corporation.

Available to DOE and DOE contractors from
U.S. Department of Energy
Office of Scientific and Technical Information
P.O. Box 62
Oak Ridge, TN 37831

Telephone: (865)576-8401
Facsimile: (865)576-5728
E-Mail: reports@adonis.osti.gov
Online ordering: http://www.osti.gov/bridge

Available to the public from
U.S. Department of Commerce
National Technical Information Service
5285 Port Royal Rd
Springfield, VA 22161

Telephone: (800)553-6847
Facsimile: (703)605-6900
E-Mail: orders@ntis.fedworld.gov
Online order: http://www.ntis.gov/help/ordermethods.asp?loc=7-4-0#online

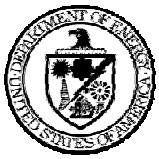

SAND2005-0860
Unlimited Release
Printed February 2005

Solution-Based Nanoengineering of Materials

Z. Ryan Tian, Louise Criscenti, Erik Spoerke, Bonnie McKenzie,
Randy Cygan, Jun Liu, and James Voigt

Sandia National Laboratories
P.O. Box 5800
Albuquerque, NM 87185-1411

Michael L. Machesky

Watershed Science Section, Illinois State Water Survey
Champaign, IL

ABSTRACT

Solution-based synthesis is a powerful approach for creating nano-structured materials. Although there have been significant recent successes in its application to fabricating nanomaterials, the general principles that control solution synthesis are not well understood. The purpose of this LDRD project was to develop the scientific principles required to design and build unique nanostructures in crystalline oxides and II/VI semiconductors using solution-based molecular self-assembly techniques. The ability to synthesize these materials in a range of different nano-architectures (from controlled morphology nanocrystals to surface templated 3-D structures) has provided the foundation for new opportunities in such areas as interactive interfaces for optics, electronics, and sensors. The homogeneous precipitation of ZnO in aqueous solution was used primarily as the model system for the project. We developed a low temperature, aqueous solution synthesis route for preparation of large arrays of oriented ZnO nanostructures. Through control of heterogeneous nucleation and growth, methods to predicatively alter the ZnO microstructures by tailoring the surface chemistry of the crystals were established. Molecular mechanics simulations, involving single point energy calculations and full geometry optimizations, were developed to assist in selecting appropriate chemical systems and understanding physical adsorption and ultimately growth mechanisms in the design of oxide nanoarrays. The versatility of peptide chemistry in controlling the formation of cadmium sulfide nanoparticles and zinc oxide/cadmiun sulfide heterostructures was also demonstrated.

ACKNOWLEDGEMENTS

The authors would like to acknowledge the contributions to the project made by Sandian's Diana Moore, Matthew McDermott, Paul Clem, Eric Coker, Tim Boyle, and Mark Rodriguez. We also acknowledge Huifang Xu and Hiromi Konishi from the Department of Earth and Planetary Sciences, University of New Mexico for their excellent TEM work.

This work was supported by Sandia National Laboratories Laboratory-Directed Research and Development Program (LDRD). Sandia is a multiprogram laboratory operated by Sandia Corporation, a Lockheed Martin company, for the U. S. Department of Energy under contract DE-AC04-94AL85000.

CONTENTS

FIGURES

TABLES

INTRODUCTION

Extended and oriented nanostructures are desirable for many applications, but direct fabrication of complex nanostructures with controlled crystalline morphology, orientation and surface architectures remains a significant challenge. Here we report a low temperature, environmentally benign, solution based approach to prepare complex and oriented ZnO nanostructures and systematically vary the crystal morphology *(Section: Solution Growth of ZnO Nanostructures)*. Using controlled seeded growth and simple citrate anions that selectively adsorb on ZnO basal planes as the structure-directing agent, we prepared large arrays of oriented ZnO nanorods with controlled aspect ratios, architectured films made of oriented nanocolumns and nanoplates that are remarkably similar to biomineral structures in red abalone shells, and complex bilayers showing in-situ column-to-rod morphological transitions. The advantages of the architectured ZnO for photocatalytic decompositions of volatile organic compounds (VOC) were demonstrated. The novel ZnO nanostructures are expected to have great potentials for sensing, catalysis, optical emission, piezoelectric transduction, actuations, etc.

We have developed representative periodic models for the two primary zinc oxide growth surfaces, (100) and (001), to understand how various adsorbates, including citrate and ethylene diamene will affect crystal growth and nanocrystalline morphologies *(Section: Molecular Simulations of Organic Cation and Anion Adsorption onto Zinc Oxide Surfaces)*. Surface oxygens were protonated as expected in an aqueous solution at 25^{o}C and pH 7 according to the revised multi site complexation (MUSIC) model. Three-dimensional molecular dynamics calculations were used to investigate the adsorption of each organic ion on both zincite surfaces. Each zinc oxide surface was initially minimized *in vacuo* to allow for complete surface relaxation. Then each zincite surface was placed in contact with aqueous solution containing the charged adsorbate and counterions. Molecular dynamics simulations of these heterogeneous systems involving a zincite surface slab, water molecules and solute ions were performed to investigate the propensity for each organic ion to adsorb to the (001) and (100) surfaces. Our computational results are consistent with experimental observation, and support the argument that the preferential binding of adsorbates, acting as growth inhibitors, may be used to design customized zincite morphologies.

We have also explored the use of engineered synthetic peptides to regulate the synthesis of semiconductor nanocrystals and their integration into heterostructures. This work was undertaken as means to determine the applicability of simple bio-inspired peptide structures to the nanoengineering of technologically important materials (*(Section: Peptide Modified Structures)*.

SOLUTION GROWTH OF ZnO NANOSTRUCTURES

Background

Extended and oriented nanostructures are desirable for many applications, including microelectronic devices, chemical and biological sensing and diagnosis, energy conversion and storage (photovoltaic cells, batteries and capacitors, and hydrogen storage devices), light emitting display, catalysis, drug delivery, separation, and optical storage. In the literature, oriented carbon nanotubes[1,2] and oriented ZnO nanorods[3-10] were prepared by high temperature vacuum deposition techniques. Similar techniques were used for making nanowires of Si[10] and silicon carbide/nitride,[12] and nanobelts of a wide range of oxide materials.[13] Recently, hydrothermal solution synthesis[14,15] and electrochemical deposition in porous membranes[16-18] were also investigated to produce oriented ZnO nanorods and tubes. Although oriented nanowires and nanorods have attracted wide attention, direct fabrication of large arrays of complex nanostructures with controlled crystalline morphology, orientation and surface architectures remains a significant challenge.

We developed a low temperature, environmentally benign, solution based method to prepare complex ZnO nanostructures. ZnO is an important wide band gap semiconducting ceramic material with many useful properties[19] such as piezoelectricity, conductivity, optical adsorption and emission, high voltage-current nonlinearity sensitivity to gases and chemical agents, and catalytic activity.[20] It has been extensively investigated for luminescence applications, [4,13,21,22] window and electrode materials for solar cells,[23] phosphors,[24] piezoelectric transducers and actuators,[25] surface acoustic coatings,[26] varistors,[27] microsensors,[28] photocatalsyts,[29] etc. The properties of the ZnO greatly depends on the microstructures of the materials, including crystal size, orientation and morphology, the aspect ratio, and even the crystalline density. The surface area and the architecture (how the crystals are stacked) also play a critical role in many applications (photo-emitters, transducers, actuators, varistors, sensors, and catalysts).

Procedure

We used a seeded growth procedure we first developed[30] to control the nucleation event, and citrate molecules to control the crystal morphologies. We chose citrate molecules because they strongly adsorb to metal[31] and mineral surfaces,[32] and significantly alter the surface properties[33,34] and mineral growth behavior.[35] The use of small citrate molecules will also allowed us to develop molecular modeling (see Section: *Molecular Simulations of Organic Cation and Anion Adsorption onto Zinc Oxide Surfaces*) to enhance our understanding on how these organic molecules bind to the different ZnO surfaces and affect crystal growth. Organic molecules are known to either promote or inhibit crystal growth. Although organic additives have been extensively investigated to modify crystal growth,[36] this strategy has not been used for the preparation and systematical control of the microstructure of large arrays of oriented nanomaterials.

Deposition of uniform coating of ZnO nanoparticles as nucleation seeds: 1 g ZnO nanoparticles (Alfa Aesar, 24 nm to 71 nm based on manufacturer's specification) was dispersed in 10 g Di-H_2O. 0.0388 g of Sokalan CP10 (BASF), a modified polyacrylic based dispersant, was added. This suspension was vigorously stirred, followed by a centrifugation at 3000 rpm for 5 min to remove coarse agglomerates. A glass slide was dipped in the remaining suspension to apply a thin ZnO coating, then air dried.

Growth of oriented nanowires (Fig. 1, Fig. 2): The glass slide containing the ZnO nanoparticle coating was vertically placed in a sealed Teflon bottle, containing 30 ml aqueous solution of $Zn(NO_3)_2$ (0.01-0.06 M) and hexamethyltetramine (HMT) (0.001 M). The reaction was carried out at 60 ^{o}C for up to three days.

Control of aspect ratio of ZnO crystals: A glass slide (without ZnO nanoparticle coating) was placed in a typical $Zn(NO_3)_2$ solution containing different amounts of sodium citrate, and reacted in a sealed Teflon container at 60°C for 3 days to produce ZnO crystals with different aspect ratios (Fig. 3a, Fig. 3b). The ZnO crystals shown in Figure 3b (grown by adding 1.5 mg sodium citrate in 30 ml solution) was placed in a fresh 30 ml solution containing 0.1 M HMT, 0.03 M $Zn(NO_3)_2$, 9.5 mg of sodium citrate, and then reacted at 95 ^{o}C for one day. Such a secondary growth introduced parallel nanoplates on the ZnO rod columnar surfaces (Fig. 3d, Fig. 3e). A third growth was performed without citrate to "heal" the plate-like nanostructure (Fig. 3f).

Control of aspect ratio of oriented rods: The oriented nanowires shown in Figure 1 were placed in a 30 ml fresh solution containing 0.003 M $Zn(NO_3)_2$, 0.03 M HMT, and 1.5 mg of sodium citrate. This process was repeated if desired.

Preparation of biomimetic nanostructures: (1) The glass substrate with the oriented ZnO rods (corresponding to Fig. 4b and Fig. 4c) was placed in a solution containing 0.030 M $Zn(NO_3)_2$, 0.10 M HMT, and 1.5 mg sodium citrate, and then reacted at 95°C for 1 day to form microstructures corresponding to Figures 5a through 5b. (2) The nanowires corresponding to Figure 1a were reacted in a 30 ml fresh solution containing 0.030 M $Zn(NO_3)_2$, 0.03 M HMT, and 9.5 mg sodium citrate, and then reacted at 60 °C for 2 days to produce the bilayer structure in Figures 5e and 5f.

Results and Discussion

Figures 1a through 1c show the scanning electron microscopy (SEM) images of large arrays of oriented ZnO nanorods formed by seeded growth. Figure 1a is a low magnification face-on image showing the uniformity of the microstructure. The hexagonal nanorods and the {001} planes can be observed at a higher magnification (Fig. 1b). The diameters of the nanorods are about 250 nm, and the length of the nanorods is about 3 μm (judged from cross-section, not shown here). A SEM image of a tilted sample reveals that most of the nanorods are highly oriented (Fig. 1c). In contrast, the same conditions without ZnO nanoparticle seeds produced sparsely populated (Fig. 1d), randomly oriented large ZnO rods, about 1 μm in diameter and 10 μm in length. This result suggests that a high density of nucleation sites is critical for growing large arrays of oriented nanorods.

In order to understand how the arrays of oriented nanorods were formed, we studied the growth kinetics by SEM and X-ray diffractometry (XRD). As shown in Figure 2, in early stages of the crystal growth, oriented structures were not formed. Figure 2a shows a SEM image of the ZnO nanoparticle seeds after 30 minutes of the crystal growth, with little sign of crystal growth. These particles mostly consist of rounded rectangular and rod shaped crystals with a wide size distribution. After one hour (Fig. 2b) of the growth, surface roughness became visible on the ZnO seeds, indicating the initiation of the crystal growth. After 3 hours, short and faceted hexagonal rods were observed (Fig. 2c), although most of these rods were not well aligned yet. The arrows in Figure 3c point to a few ZnO nanorods that start to grow in the vertical orientation. XRD results (Fig. 2d) confirmed that the ZnO crystals are hexagonal wurtzite structure ($P6_3mc$, a = 3.2495 Å, c = 5.2069 Å). The results from 1 to 5 hours are characteristic of randomly oriented ZnO powders, showing the (100) and (101) reflections as the main peaks. The (002) reflection was only significantly enhanced after extended growth, indicating that the ZnO were mostly randomly oriented at the beginning, but became <001> oriented after a long time growth.

Results presented in Figure 2 suggest the following three steps for growing oriented ZnO nanorods (inset in Fig. 2d): (1) deposition of crystal seeds on the substrate surface, (2) growth of randomly oriented crystals from the seeds, and (3) growth of aligned nanorods after extended reactions. In the early stages of growth, ZnO crystals grew along the fastest growth orientation, the <001> direction, and these crystals were not aligned. However, as the rod-like crystals grew further, randomly oriented crystals began to overlap and their growth became physically limited as the misaligned nanorods began to impinge on other neighboring crystals, giving rise to the preferred orientation of the film. In the absence of the nucleation seeds, ZnO crystals were sparsely nucleated on the substrate. These crystals had freedom to grow in all orientations to large sizes (Fig. 1d).

We studied the effect of citrate on ZnO crystal morphology. Figure 1d and Figure 3 show typical ZnO crystals grown on glass surfaces at different citrate concentrations. Without citrate ions, long ZnO rods were formed (Fig. 1d). When a very small amount of citrate ions was added, the ZnO rods became shorter and fatter (Fig. 3a), and the aspect ratio (height/width) was rapidly decreased. Further additions of citrate ions caused the formation of short and fat hexagonal crystals (Fig. 3b). On the average, the aspect ratios of the crystals were directly related to the citrate concentrations (Fig. 3c). This systematic correlation suggests that citrate ions slowed down the crystal growth along the <001> orientation, and therefore provided a simple approach to control the aspect ratio of the ZnO nanorods.

We have further demonstrated that much higher citrate concentrations can produce plate-like ZnO crystals, rather than rod-shaped particles. We used the crystals in Figure 3b as the seeds, and performed a secondary growth with a high citrate concentration. Although the new crystals in Figures 3d and 3e retained the hexagonal shape, layered features were observed on the crystal surface, suggesting that crystal growth along <001> orientations was suppressed under these conditions, but the crystals were still allowed to grow side-wise in the form of thin platelets. The transition from long hexagonal rods to short hexagonal crystals, and then to hexagonal crystals containing stacked nanoplates along

with the increase in citrate concentration, is illustrated in the inset in Figure 3c. Here the platelets are also quite uniform in thickness (about 5 to 10 nm) throughout the sample. On the other hand, if the crystals in Figures 3d and 3e were used as the seed crystals and placed in a solution without citrate ions, the <001> growth behavior was restored and the 5 to 10 nm layered features were mostly "healed" (Fig. 3f), with the exception of some large gaps in between the nanoplates. Figures 3d through 3f are among the first examples to demonstrate reversible in-situ rod-to-plate morphology transitions in synthetic ceramics, which morphologically resembles the rod-to-plate transition in abalone shells using calcite and aragonite generating proteins. Recently Taubert et al. reported that certain polymers had a large effect on ZnO crystals precipitated in the solution.[37,38] Diblock copolymers containing ethylene oxide, styrene and sulfonic acid groups caused the formation of complex "stack of pancakes like" ZnO particles. However, the work by Taubert et al. did not show oriented structures and systematic control of the morphology.

To systematically vary the aspect ratios of the oriented ZnO crystals, we used the oriented ZnO nanorods as shown in Figures 1a through 1c as the starting materials, and performed secondary and tertiary growths in the presence of citrate ions. Figure 4 shows the continuous change of the aspect ratios of oriented rods using this approach. As compared with Figure 1, the ZnO rods became much thicker (over 0.5 μm) after the secondary growth, but not much longer (still about 3 μm, as revealed by the cross-sectional SEM image in Fig. 4b) because the growth along <001> orientation was inhibited by the citrate binding. After a tertiary growth, the surface became densely populated with thick oriented ZnO rods, more than 0.8 μm in diameter (Fig. 4d). On the other hand, it is important to point out that if the secondary and tertiary growths were conducted without citrate, the overall crystal sizes increased. At the same time, both the diameter and the length of the crystals were increased.

By using multiple step seeded nucleation and growth, and using high citrate concentrations, we were able to prepare a variety of large arrays of ZnO nanostructures that are remarkably similar to those from biogenic calcium carbonates. In nature, biomaterials like seashells use biomolecules to achieve precise controls of the orientations and morphologies that are not commonly observed in synthetic materials.[39,40] Developing synthetic approached to prepare such complex oriented nanostructures remains a significant challenge. Figures 5a and 5b show the column-like growth of ZnO plates. The nanoplates and the plate-like nanowires[30a] grew on top of the oriented ZnO nanorods. As discussed earlier, ZnO normally has a rod-like morphology. The growth of oriented nanoplates is quite unusual, and is directly related to the function of the organic acid (citrate) that inhibited the longitudinal growth of rods but promoted the growth of plates. As a comparison, SEM images of nacre in *Haliotis rufescens* (red abalone) are shown in Figures 5c and 5d. However, we do not imply that biominerals and ZnO nanostructures are formed through exactly the same mechanism, but the similarities of these morphologies are quite striking.

We can also take advantage of the column-to-plate transition to prepare oriented bilayer structures. We first grew the oriented arrays of ZnO nanorods as shown in Figure 1. Then we performed the secondary growth at a much higher citrate concentration. Under this condition, the formation of plate-like ZnO crystals on top of the rods dominate the crystal

growth. This process produced a bilayer structure containing first layer of ZnO nanorods, and second layer of ZnO nanoplates (Fig. 5e, Fig. 5f).

We performed detailed transmission electron microscopy (TEM) study on the ZnO nanostructures using a JEOL 2010 FEG STEM/TEM operated at 200 KV. Figure 6a with the inset shows bright-field (BF) TEM images of a column corresponding to the nanocolumns shown in Figure 5c, and Figure 6b shows the $<1\bar{1}0>$ zone-axis selected-area electron diffraction (SAED) pattern. The single crystal SAED pattern suggests that all the ZnO nanoplates are aligned in both *c* and *a* directions. The longitudinal direction is along the <001> orientation. A high-resolution TEM (HRTEM) image shown in Figure 6c reveals the 5 to 10 nm thick nanoplates, as well as the 2.6 Å {002} lattice fringe parallel to the basal plane. Figure 6d shows a <001> zone-axis HRTEM image. Here the six fold symmetry and the 2.8 Å {100} lattice fringes in three directions are clearly resolved. The TEM results also suggest that at least in the early growth stage the nanoplates are single crystalline. However, a careful analysis of the SAED patterns and HRTEM images suggest a slight misalignment in between, or even within the plates. The exact amount of misorientation seems to vary slightly from area to area and is still being analyzed.

Our synthetic approach has enabled us to produce a wide range of unusual complex microstructural features that are remarkably similar to that in biomaterials. We hope that the oriented nanostructures in engineering ceramics with controlled orientation, crystal size, morphology, surface area, and defect structures would be useful in many applications discussed earlier. As a preliminary experiment, we tested photocatalytic properties of different microstructures in photodecompositions of volatile organic compounds (VOC), an important application for "green" treatment of wastewater. We placed glass substrate supported ZnO samples into 10 ml aqueous solutions containing 30 ppm 4-chlorophenol and then exposed the sealed solutions to natural sunlight. Without the ZnO catalyst, no significant change was detected after 2.5 hours. With the vertically oriented ZnO rods (corresponding to Fig. 1a) as the catalyst, the 4-chlorophenol concentration was reduced by 14% after the same period of time. Under the same condition, but with the architectured ZnO (corresponding to Fig. 5c) as the catalyst, the 4-chlorophenol concentration was reduced by 25%. The enhanced catalytic property could be attributed to the high surface area, and/or the unique surface nanofeatures. These preliminary results suggest that the novel ZnO nanostructures we have prepared could have environmental and industrial applications.

Conclusion

In conclusion a low temperature, aqueous solution synthesis route to systematically prepare large arrays of oriented ZnO nanostructures by controlling heterogeneous nucleation and growth, and to predicatively alter the ZnO microstructures by tailoring the surface chemistry of the crystals. Also as part of this project, we have demonstrated that

this synthetic approach could also be applied to prepare other oriented nanostructures, such as oriented TiO_2 nanotubes.[41]

MOLECULAR SIMULATIONS OF ORGANIC CATION AND ANION ADSORPTION ONTO ZINC OXIDE SURFACES

Background

The control of ZnO morphology described in the previous section relies on the preferential adsorption of the citrate anion onto growth surfaces to control the morphology. Anions other than citrate, as well as neutral aqueous species, were also tested in the laboratory for their potential use in controlling zinc oxide growth morphology. Unlike the other adsorbates, citrate exhibits particularly strong preferential adsorption to the (001) surface, and therefore provides a valuable control on the design of zincite nanostructure arrays. With increasing citrate concentration in solution, the zinc oxide crystals evolve from long prismatic crystals to those that are more platey. Representative zinc oxide morphologies are illustrated in Fig. 3. In contrast, experiments using a cation, ethylene diamine, suggest that this adsorbate binds preferentially to the (100) surface inhibiting zincite growth in this direction.

The molecular simulation of the adsorption of neutral molecules, anions, and cations onto zincite surfaces may provide a powerful predictive capability to help guide the experimental studies. In this section, we examine the adsorption of ethylene diamine and citrate onto different zincite surfaces using classical molecular dynamics (MD) simulations, to test our ability to computationally predict the experimental results. First, we prepare molecular models of the (001), $(00\bar{1})$, and (100) zincite surfaces and the two adsorbates, that are protonated according to known or predicted pKs for aqueous conditions at 25°C and pH 7. Then, we use 3-D MD simulations to examine the energetics and geometries of both aqueous and adsorbed citrate and ethylene diamine. Adsorption onto the $(00\bar{1})$ surface is examined although ZnO crystal growth in assumed to occur in the (001) direction. This assumption is supported by numerous experimental observations including those of Demainets and Kostomarov[42] who report that the growth rate of ZnO in the (001) direction is 1.5-2 times larger than that in the $<00\bar{1}>$ direction and Li et al.[43] who report that under hydrothermal (200-350°C) conditions, the maximal crystal growth velocity is fixed in the *<001>* direction and the relationship between the velocities of crystal growth in different directions is V*<001>* > V*<010>* > V$<00\bar{1}>$.

Our MD simulations support the preferential adsorption of citrate onto the (001) growth surface and the adsorption of ethylene diamine to the (100) growth surface observed experimentally.

Computational Approach

Surface Construction and Adsorbate Selection

Three-dimensional periodic lattice models of the zinc oxide surfaces were generated from the unit cell structure using Cerius^2 software (Accelyrs, Inc.; Sabine and Hogg[44]). The (100) periodic slab is approximately 26 Å long, 16 Å wide, and 17 Å deep, while the (001) periodic slab is approximately 28 Å long, 16 Å wide, and 13 Å deep. Each slab is separated from the next periodic image by a 30 Å vacuum gap. The ZnO surface slabs were first minimized in vacuum prior to incorporating an MD-equilibrated water box (28 Å deep) into the 30 Å gap.

The oxygens on each surface were protonated as they would occur by hydrolysis reactions in aqueous solution at 25°C and pH 7 according to the revised multi site complexation (MUSIC) model.[45,46] In this model, the bond valence *s* is based on the metal (*Me*)–oxygen (O) distances within a crystal structure according to the expression:

$$s = e^{-(R-R_o)/b}$$

in which R is the *Me*-O distance, R_o is an element-specific distance, and b is a constant (b = 0.37 Å). The value of R_o was obtained by analysis of the bond valence structure of many metal-oxygen bonds in crystals,[47] such that the sum of the actual bond valence $\sum s_j$ around an oxygen, based on the known distances R, is equal to the valence V of the oxygen. In the revised MUSIC model, the neutralization of the oxygen charge can be calculated from the contributions *s* by the *Me* ion, the H-occupied (*m*) and the unoccupied (*n*) orbital(s), according to:

$$V \neq -\sum s_j = -\{s_{Me} + ms_H + n(1-s_H)\}$$

where s_H is the bond valence of the H-donating bond and (1-s_H) the bond valence of the accepting one. Note that the charge of the surface oxygens is not fully neutralized. For ZnO, *m*=*n*=*0*, therefore:

$$V \neq -\sum s_j = -s_{Me}\,.$$

For zincite, four different types of unsaturated oxygen sites are found on the three surfaces considered, (100), (001), and $(00\bar{1})$. The saturation states of each site-type as well as the Zn-O bond lengths associated with each site-type on each surface are provided in Table 1. The (100) surface is characterized by two unique surface sites: monodentate Zn-O sites where the oxygen atoms at the surface are each bonded to one zinc atom in the bulk crystal structure, and tridentate Zn_3-O sites where the surface oxygen atoms are bonded to three zinc atoms. The MUSIC model assumes that the absolute value of the charge of a surface site in aqueous solution is less than or equal to one. Depending on the charge of the unsaturated oxygen, surface sites can then be singly- or doubly-protonated. For example, the protonation reactions for the two site-types on the (100) surface are:

$$Zn-OH^{-0.494} + H^+ \leftrightarrow Zn-OH_2^{+0.506}$$

and

$$Zn_3-O^{-0.506} + H^+ \leftrightarrow Zn_3-OH^{+0.494}$$

The (001) surface is characterized by only one type of surface site: a monodentate Zn-O site that is distinct from that found on the (100) surface of ZnO. The difference between these monodentate sites lies in the distance between the surface oxygen atom and the underlying zinc atom. On the (100) surface, the Zn-O bond length is 1.973 Å long. The

bond distances are derived from the bulk zinc oxide crystal structure.[44] In contrast, on the (001) surface, the Zn-O bond length is 1.992 Å. While the difference in bond lengths does not change the stoichiometry of the protonation reaction, it does result in slightly different charges on the surface sites:

$$Zn-OH^{-0.519}+H^{+}\leftrightarrow Zn-OH_2^{+0.481}$$

Zincite is a polar mineral where the $(00\bar{1})$ surface is substantially different in character from the (001) surface. The $(00\bar{1})$ surface is characterized by one type of site, a Zn_3-O site that is also distinct from the tridentate site found on the (100) surface due to differences in bond length. On the (001) surface, each triply-coordinated oxygen is characterized by two Zn-O bonds that are 1.973 Å long and one Zn-O bond that is 1.992 Å long. In contrast, the triply coordinated oxygen sites on the $(00\bar{1})$ surface are equidistant from three zinc atoms, each Zn-O bond is 1.973 Å long. Again, while the difference in bond lengths does not change the stoichiometry of the protonation reaction, it does result in different charges on the surface sites:

$$Zn_3-O^{-0.481}+H^{+}\leftrightarrow Zn_3-OH^{+0.519}$$

We assumed crystal growth occurs at the (001) surface, not the $(00\bar{1})$ surface and therefore did not emphasize adsorption to this surface. However, the $(00\bar{1})$ surface was protonated according to the MUSIC model for consistency.

Within the context of the revised MUSIC model, surface proton affinity constants, log *K*s, are calculated from the correlation:

$$\log K=-A(\sum s_j+V)$$

where the constant *A* is determined from a correlation between the proton affinity constants for aqueous metal-hydroxo and oxo- complexes and the undersaturation of the oxygen valence $-(\sum s_j+V)$[47]. The reactions for ZnO surface protonation and associated equilibrium constants for 25°C are summarized in Table 2. Assuming a pH of 7, the ratio of doubly-protonated to singly-protonated, or singly-protonated to unprotonated, sites for each site-type were calculated using the appropriate log *K* value. Each zincite surface was then protonated according to these ratios. For example, the log *K* for protonation of the (100) tridentate surface sites suggests that at a pH of 7, there will be one protonated site to every two unprotonated sites. Therefore, we distributed the protons evenly along the simulation surface by added a proton to every third (100) tridentate surface site.

Once the protonation scheme for each zincite surface was defined using the revised MUSIC model, the charge distribution for each three-dimensional periodic zinc oxide surface was determined using the algorithm of Rappé and Goddard.[48] Average partial charges for the Zn and O atoms for each atomic layer of the periodic slab, and for the Zn, O, and H atoms involved in each type of surface site were also calculated and substituted into the three-dimensional slab model. This approach maintains the charge neutrality of the surface model and also the distinction between the different surface site types.

The adsorption of an organic anion (citrate) and cation (ethylene diamine) on each of the ZnO surfaces was investigated. For conditions of 25°C and pH 7, the protonation state and ion charge of citrate and ethylene diamine were determined from their acidity constants to be $(COO)_3COOH(CH_2)_6$ (-3) and $H_3NCH_2CH_2NH_2$ (+1), respectively. The partial charges on the organic anions were defined using the consistent valence forcefield (CVFF[49]) that was fit to small organic crystals and gas phase structures, and handles a wide range of organic systems.

Molecular Simulations

We first tried to model the adsorption of both neutral molecules and ions to the zincite surfaces using 2-D molecular mechanics simulations of the surface and adsorbates *in vacuo*. These simulations were performed using the Universal Force Field (UFF[50]) in which the force field parameters are generated from a set of rules based on element, hybridization, and connectivity. The Coulombic interactions were calculated using a 2-D Ewald summation method included in the Cerius[2] (Accelyrs, Inc.) molecular modeling package. However, this particular algorithm[51] does not include a charge-neutralizing background, works only for neutral systems, and is inappropriate for examining systems with a neutral surface slab and a charged adsorbate.

Therefore we turned to using fully-saturated, charge-balanced, 3-D simulation cells to perform molecular dynamics calculations to investigate the adsorption of citrate and ethylene diamine to the zincite surfaces. These simulations were performed using CVFF[49] with added force field parameters for zincite that were derived using UFF.[50] Forcefield parameters were developed to describe the bond-stretch energy for Zn-O, and the angle-bend energy for both ∠Zn-O-Zn and ∠O-Zn-O angles by calculating single point energies at a series of distances and angles respectively. These energies, as a function of distance or angle size, described parabolic curves that were easily fit with the following harmonic equations:

$E_{Zn-O} = \frac{1}{2}k(x - x_o)^2$, where k = 332.14 and x_o = 1.8188,

$E_{O-Zn-O} = \frac{1}{2}k(\theta - \theta_o)^2$, where k = 169.3928 and θ_o=111.8953

and,

$E_{Zn-O-Zn} = \frac{1}{2}k(\theta - \theta_o)^2$, where k = 57.7774 and θ_o=106.3807

The bond-stretch forcefield parameters were also used to describe the zincite surface sites, where Zn is bonded to an OH group, and where a tridentate surface oxygen atom is protonated.

Non-bonded van der Waals energy expressions were also determined from single point energy calculations using UFF for Zn-Zn, O-O, and Zn-O interactions. The single point energies calculated as a function of distance between each set of two ions, were fit to a 6-12 Lennard-Jones potential:

$$E = D_o[\left(\frac{R_o}{r}\right)^{12} - 2\left(\frac{R_o}{r}\right)^{6}].$$

Good fits to this potential were determined using R_o = 3.0, and D_o = 0.0424, 0.3582, and 0.1358, for Zn-Zn, O-O, and Zn-O interactions respectively.

The total energy expression used in our simulations with the modified version of CVFF is:

$$E_{total} = E_{bond} + E_{angle} + E_{torsion} + E_{Inv} + E_{xterm} + E_{VdW} + E_{Coulomb}$$

where E_{total} is the total potential energy of the system; the bonded energy terms –E_{bond}, E_{angle}, $E_{torsion}$, E_{inv} and E_{xterm} – represent the energy associated with bond stretching, bond angle bending, torsion, inversion, and couplings between deformations of internal coordinates, respectively; and, the nonbonded terms, E_{VdW} and $E_{Coulomb}$, are the energy contributions due to van der Waals interactions and electrostatics. The van der Waals interactions are described by a Lennard-Jones potential that is attenuated by a spline function at an interaction cutoff distance of between 11 and 14 Å. Beyond this distance, van der Waals interactions are ignored. The Coulombic interactions are calculated using the 3-D Ewald summation method that accurately obtains the converged potential energy associated with long-range electrostatic forces.[52]

The following starting configurations were used for the MD simulations:

(1) The (001) and (00$\bar{1}$) surfaces with 3 Na^+ and a citrate anion in the middle of the 30 Å water gap between ZnO surface slabs.

(2) The (001) and (00$\bar{1}$) surfaces with 3 Na^+ cations in solution and the citrate anion adsorbed to the (001) surface as an inner-sphere complex, with no water molecules between the zincite surface and citrate.

(3) The (100) ZnO surface with 3 Na^+ and one citrate ion in solution.

(4) The (100) ZnO surface with 3 Na^+ cations in solution and the citrate anion adsorbed to the (100) ZnO surface as an inner-sphere complex.

(5) The (001) and (00$\bar{1}$) surfaces with 1 Cl^- and 1 ethylene diamine ion in the middle of the 30 Åwater gap between ZnO surface slabs.

(6) The (001) and (00$\bar{1}$) surfaces with 1 Cl^- ion in solution and ethylene diamine adsorbed to the (001) surface as an inner-sphere complex.

(7) The (100) ZnO surface with 1 Cl^- and 1 ethylene diamine ion in solution.

(8) The (100) ZnO surface with 1 Cl^- ion in solution and one ethylene diamine cation adsorbed to the (100) ZnO surface as an inner-sphere complex.

Results and Discussion

Figures 7 and 8 illustrate the protonated ZnO surface slabs used in the 3-D periodic MD simulations. The (001), (00$\bar{1}$), and (100) surfaces are each protonated according to the proton affinity constants (log Ks) determined from the revised MUSIC model for ZnO in an aqueous solution with pH 7 at 25°C. The relationship between the (001) and (00$\bar{1}$) surfaces is illustrated in Fig. 7A. Expanded versions of both surfaces are illustrated in

Fig. 7B. The (001) surface is characterized by doubly-protonated monodentate oxygen atoms, while the $(00\bar{1})$ surface is predominantly characterized by unprotonated tridentate oxygen atoms. These surfaces emphasize the polarity of the ZnO crystal – where the (001) $ZnOH_2$ surface groups are positively charged and the $(00\bar{1})$ Zn_3O surface groups are negatively charged. (The zincite slab is neutral). For the (100) surface illustrated in Fig. 8, the monodentate surface sites are all doubly-protonated. One-third of the triply-coordinated surface oxygens are protonated. The $(\bar{1}00)$ surface is identical to the (100) surface and therefore does not need to be discussed separately. The surface sites are systematically protonated in our models to provide a uniform distribution for each unique site-type.

In the first MD simulation for the (001) and $(00\bar{1})$ surfaces, started with the citrate anion initially centered between the two surfaces in bulk solution, the citrate anion migrated toward the positively-charged (001) surface during the 150 ps timeframe (Fig. 9A). When the citrate anion is initially placed at the (001) surface as an inner-sphere complex (Fig. 9B), it remains at that surface as an inner-sphere complex throughout the 150 ps simulation. The citrate anion diffuses along the surface, but H-bonds between the CH_2 groups of the anion to the $ZnOH_2$ surface groups are present throughout simulation. In both of these simulations, there is no strong association between the Na^+ cations and the citrate anion. However, one Na^+ cation is adsorbed as an inner-sphere complex to the (001) surface throughout both simulations.

In contrast, for the (100) ZnO surface, citrate in bulk solution does not migrate toward a surface during the simulation. In this case, both the top and bottom surfaces of the zincite slab are identical. Citrate, initially placed on the (100) surface as an inner-sphere complex, reaches a local equilibrium with part of the anion directly bound to the zincite surface, and the rest of the anion separated from the (100) ZnO surface by one layer of water molecules. The citrate anion is also associated with one of the Na^+ cations in both of these simulations. In bulk solution, the Na^+ sits between the two oxygen atoms of a carboxyl group, while at the (100) surface, the Na^+ is strongly associated with one oxygen atom from each of two carboxyl groups, and the oxygen atom of the hydroxyl group of the citrate anion.

Ethylene diamine (+1) in bulk solution may migrate a little toward the $(00\bar{1})$ during the 150 ps timeframe of the simulation, but certainly does not show the propensity to move towards this surface and adsorb that citrate exhibits for the (001) surface. Placed as an inner-sphere complex at the (001) surface, ethylene diamine rapidly moves away from the surface into bulk solution and remains there for the remainder of the simulation time. We can conclude that ethylene diamine adsorption to the (001) surface is not favored.

Ethylene diamine in bulk solution in the presence of the (100) ZnO surface remains in solution throughout the simulation. In this particular simulation, the Cl^- ion is in close proximity to ethylene diamine and the ion pair stays together for over 75 ps. When ethylene diamine is initially positioned as an inner-sphere complex on the (100) ZnO surface, it stabilizes as an inner/outer-sphere complex, in which the positively charged half of $H_3NCHCHNH_2$ is directly bound to the surface, and the neutral half of the

molecule is separated from the surface by one layer of water molecules. The ethylene-diamine cation diffuses along the surface, and seems to oscillate between a more linear and a more folded configuration. In a second simulation with ethylene diamine at the (100) surface, the Cl^- ion formed an inner-sphere complex at the surface, and the organic cation promptly migrated away from the surface. In a third simulation with three times the concentration of ethylene diamine and Cl^- in the simulation cell, one ethylene diamine cation and one Cl^- anion bind to the (100) zincite surface.

Table 3 presents the average potential energies for each simulation and the difference between these energies for the systems with the organic ion in solution and adsorbed to a ZnO surface. In three of the four comparisons, the organic ion is equally stable in bulk solution and at the ZnO surface. However, ethylene diamine was not stable at the (001) surface.

The most intriguing result from the present molecular modeling study is our success in matching the experimental result that citrate binds much more strongly to the (001) zincite surface than to either the $(00\bar{1})$ or (100) surfaces. The experiments demonstrate a strong growth inhibition on the (001) surface leading to a more platy ZnO morphology. Citrate adsorption to the (001) surface occurs through two of the three carboxylate groups and the hydroxyl group. Each oxygen atom in the two carboxylate groups is between 2.5 Å and 3.0 Å away from three or four of the hydrogen atoms bound to the (001) surface. In one of the engaged carboxylate groups, one oxygen atom is equidistant from both hydrogen atoms of a doubly-protonated surface site. This implies that the carboxylate group will no longer be symmetrical with a delocalized electron equally shared between the two oxygens. The remaining three oxygen atoms of the two carboxylate groups interacting with the surface are equidistant to at least three of the surface sites. The hydroxyl group is pointed down toward the surface; the hydrogen atom is between 4 and 5 Å away from several surface sites and approximately 6.5 Å above a four-fold oxygen atom within the first layer of the zinc oxide structure.

Conclusion

This study demonstrates that molecular mechanics simulations, involving single point energy calculations and full geometry optimizations, can assist in selecting appropriate chemical systems and understanding physical adsorption and ultimately growth mechanisms in the design of oxide nanoarrays. Our success in matching experimental results for controlling zinc oxide crystal growth morphology from aqueous solution suggests the usefulness of molecular simulations in predicting the relative binding and therefore potential utility of different adsorbates in designing these nanosystems. Although more rigorous simulations (e.g., electronic structure or water solvation) may help to refine the simulations of this study, they would be computationally prohibitive. In contrast, we present a fairly cost-effective simulation approach to rapidly test and compare the relative binding strengths of several candidate growth inhibitors onto fully relaxed oxide surfaces, and that effectively describes the dominant mechanism that controls adsorption.

PEPTIDE MODIFIED STRUCTURES

The versatility of peptide chemistry has allowed us to create a series of multifunctional molecules whose structures are based on a "tree" model. (See Figure 10) The branches of the tree consist of a dendritic arrangement of amino acids such as cysteine, histidine, or lysinewhich interact strongly with metal ions such as cadmium or zinc, primary constituents of semiconductors such as cadmium sulfide and zinc oxide. The trunk and roots of the tree model comprise more structurally functional amino acids such as strongly charged aspartic acid or the bioderived dihydroxyphenylalanine (DOPA) commonly found in adhesive proteins of aquatic creatures such as mussels.

Our studies have shown that a peptide whose branches are made from either cysteine or histidine and whose roots comprise aspartic acid residues make excellent capping agents for the aqueous synthesis of blue-emitting fluorescent cadmium sulfide nanocrystals. Interestingly, the fluorescence of nanocrystals created by these engineered dendritic peptides is distinct from using cysteine or histidine alone as shown in Figure 11. While cysteine and histidine alone produce green and yellow fluorescent CdS respectively, the engineered peptides produce blue fluorescent nanocrystals. These differences are believed to be due to the differences in the capping ability of the peptide and demonstrate one form of applicable control these versatile peptide compounds may exert over the synthesis of semiconductors and their properties.

The same molecular tree motif has been useful in creating zinc oxide, cadmium sulfide heterostructures. The bioderived DOPA molecule has been shown to have a particular adhesive affinity for zinc oxide. We have shown that films of peptides with DOPA roots and cysteine branches may be adhered to hexagonal zinc oxide rods grown off of glass surfaces. As seen in Figure 12, this lysine-functionalized DOPA molecule demonstrates promising selectivity for the zinc oxide surfaces. The red fluorescent emission from the peptide corresponds very closely with the yellow fluorescence of the zinc oxide in Figure 12. The use of lysine in the branched element of this molecular design, coupled with the use of DOPA in the roots of the molecule have allowed us to create highly amine-functionalized zinc-oxide surfaces. This approach allows us to consider functionalization of zinc oxide surfaces in much the same way that aminosilanes have been applied to silica-based surfaces and aminothiols have been used to aminate gold surfaces. This amine functionalization provides a valuable chemical handle on semiconducting ZnO surfaces which has already shown promise in sensor applications and multicomponent materials assembly using biological microtubules. In other cases, incorporation of cysteines into the DOPA peptide (Figure 13) has shown promise in directing the growth of cadmium sulfide nanocrystals on zinc oxide crystals such as those indicated by the red arrows in Figure 13.

FIGURES

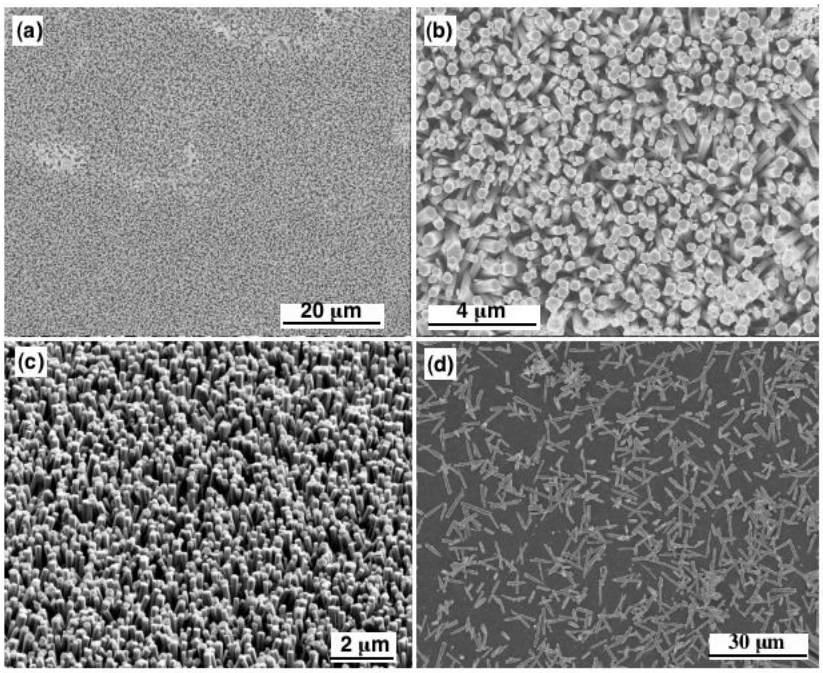

Figure 1. SEM images of large arrays of oriented ZnO nanorods using seeded growth without citrate addition. a, Low magnification, face-on view. b, High magnification, face-on view. c, A SEM image of a tilted sample. d, Randomly oriented ZnO rods without using the pre-coated ZnO nanoparticles as seeds.

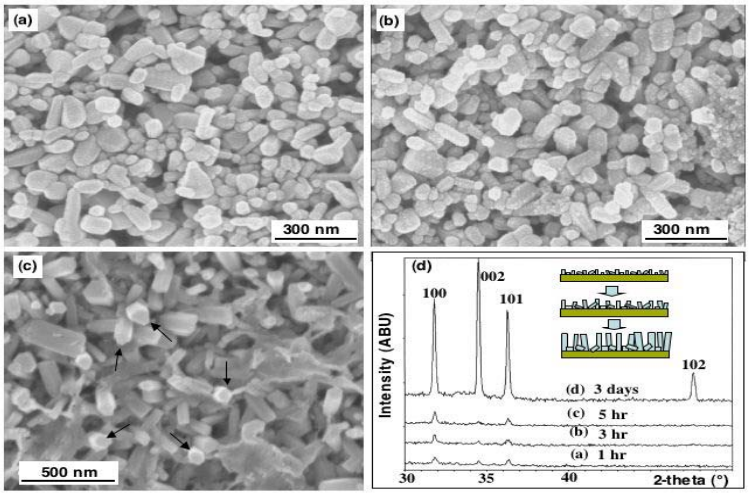

Figure 2. ZnO growth as a function of time. a, ZnO seed particles on the glass substrate after 30 minutes of reaction. b, Roughened ZnO particles after 1 hour of growth. c, Facetted ZnO rods after 3 hours of growth. d, XRD patterns of the ZnO films as a function of time. The inset in Figure 2d is a schematic illustration of the growth process.

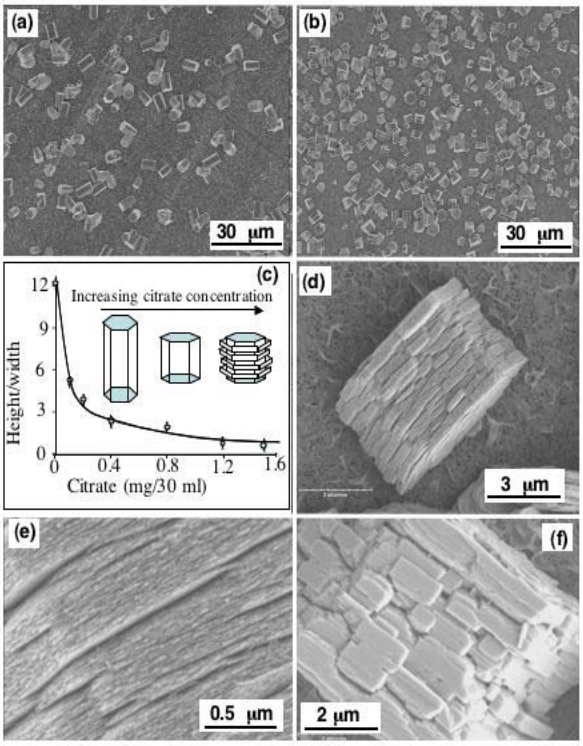

Figure 3. ZnO crystal morphology as a function of citrate concentrations. a, ZnO with 0.2 mg sodium citrate in 30 ml solutions. b, ZnO with 1.5 mg sodium citrate in 30 ml solutions. c, Aspect ratios (height/width) as a function of citrate concentrations. d, Secondary growth with citrate from b. e, High magnification SEM image of 5-10 nm plate-like nanofeatures on the (100) surfaces of the crystals. f, "Healing" of the plate-like nanofeatures after a reaction without citrate ions.

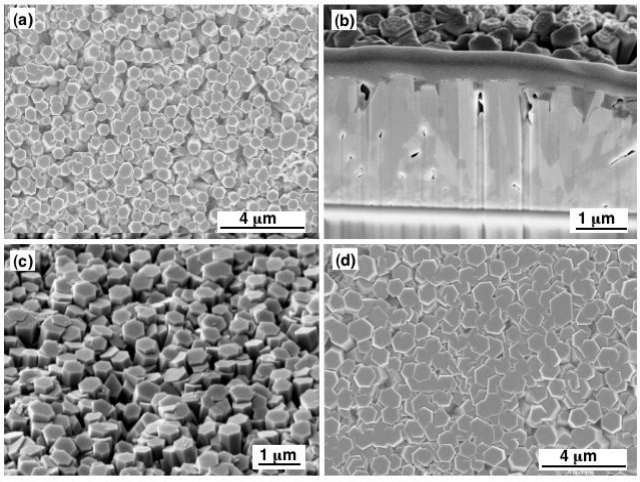

Figure 4. Control of aspect ratio of large arrays of oriented ZnO rods through secondary and tertiary growths in the presence of citrate. a, Face-on view of arrays of thick ZnO rods through secondary growth. b, Cross-sectional view of a. c, Tilted view of a. d, ZnO rods after tertiary growth in citrate solutions, face-on view.

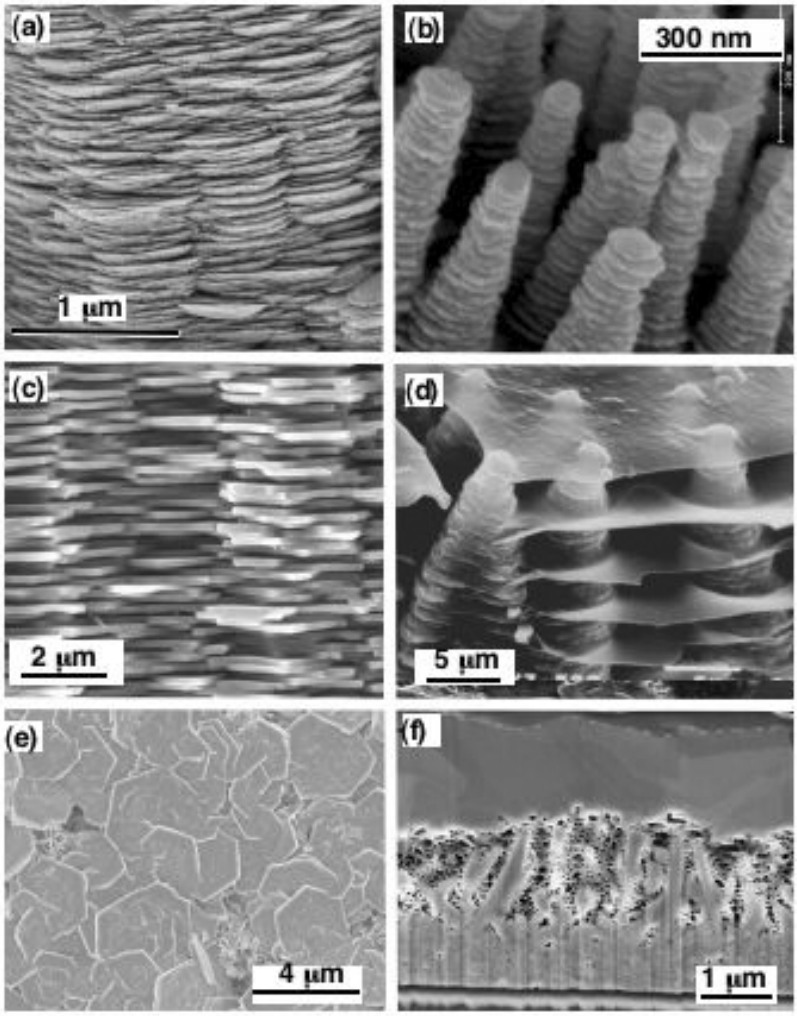

Figure 5. Oriented biomimetic ZnO nanostructures. a, Oriented ZnO nanoplates. b, Growth tip of oriented ZnO columns and plates. c, Nacreous plate structure in red abalone.d, Nacreous calcium carbonates columns and layers near the growth tip of a young abalone. e, Plate-like structures on top of ZnO bilayers. f, Column-to-plate transition in the ZnO bilayers.

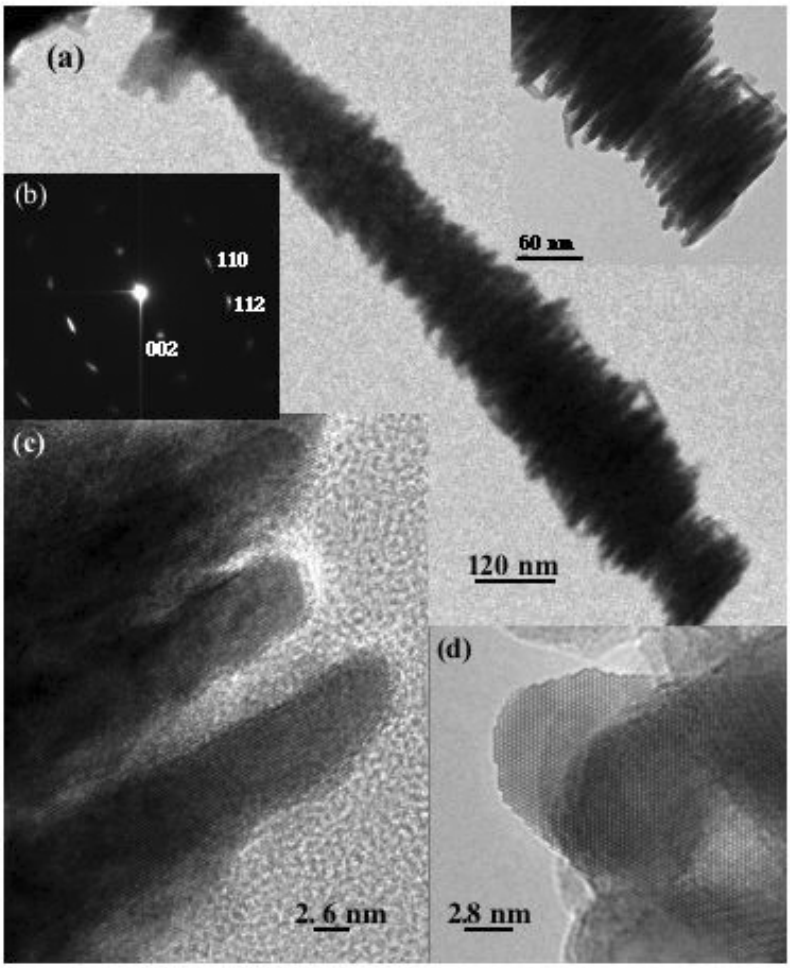

Figure 6. Representative TEM results of the ZnO nanostructures. a, Bright-field TEM images of a nanocolumn. The inset is a higher magnification image of the nanocolumn. b, A $[1\,\bar{1}\,0]$ zone-axis diffraction pattern for Figure 1a. c, A HRTEM image of the nanoplates showing the 2.6 Å {002} lattice fringes. d, A <001> zone-axis HRTEM image of the nanoplates.

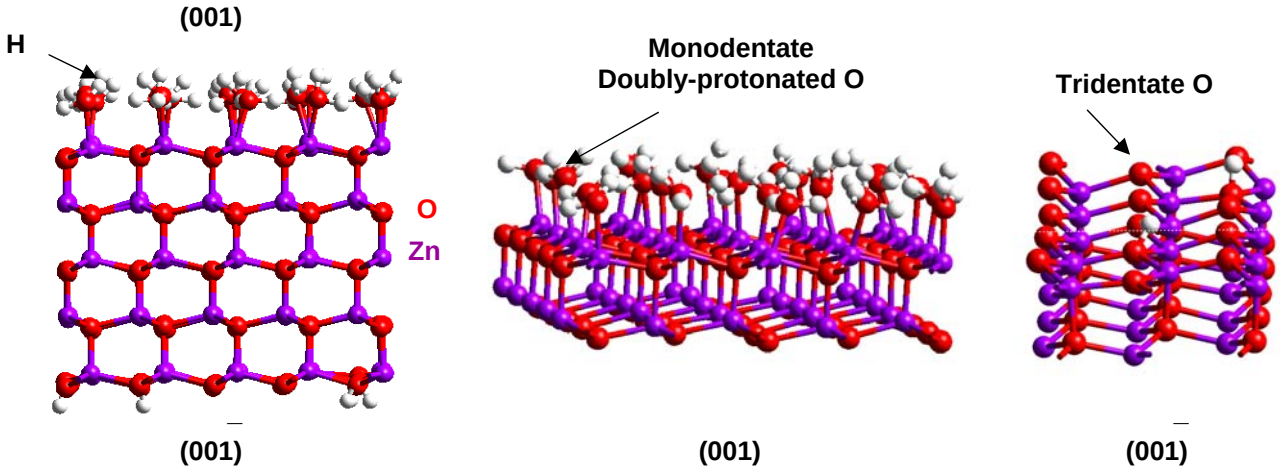

Figure 7. Diagrams of the slab model used to represent the (001) and $(00\bar{1})$ ZnO surfaces. The slab model used in the 3-D periodic simulation cell exposes both of these surfaces due to the polarity of the ZnO crystal. On the (001) surface all exposed oxygens are only bonded to one Zn atom within the bulk crystal structure. On the $(00\bar{1})$ ZnO surface, the oxygen atoms are all bonded to three Zn atoms within the ZnO crystal structure. According to the revised MUSIC model, at 25°C and a pH 7, the monodentate (001) oxygen atoms are all doubly-protonated, while most of the tridentate $(00\bar{1})$ oxygens are unprotonated

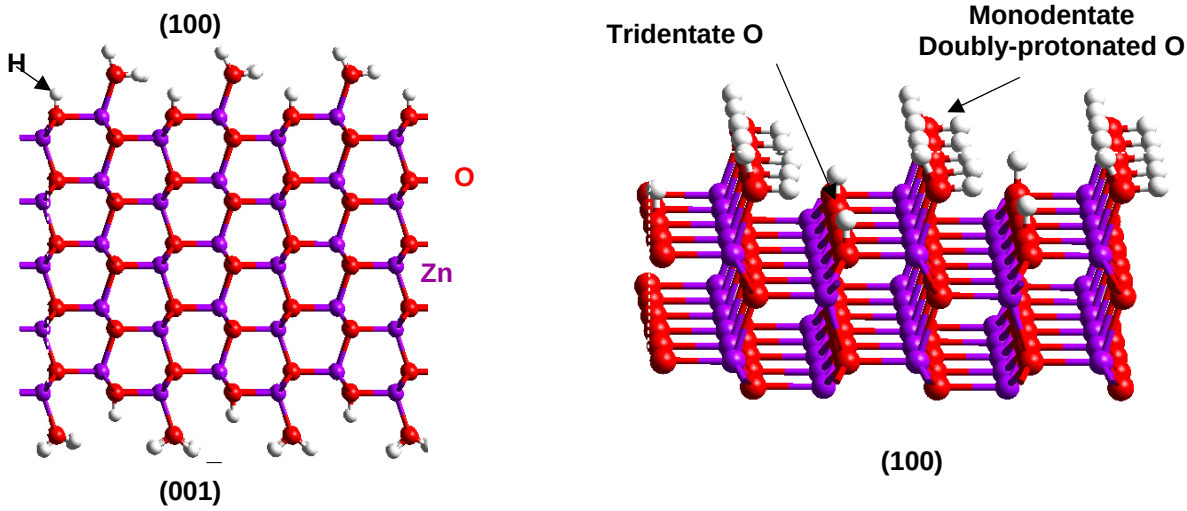

Figure 8. Diagrams of the slab model used to represent the (100) and $(\bar{1}00)$ surfaces which are identical due to the symmetry of the ZnO crystal. These surfaces are characterized by both monodentate and tridentate oxygen atoms. According to the revised MUSIC model, at 25°C and a pH 7, the monodentate oxygen atoms are doubly-protonated and one-third of the tridentate oxygen atoms are singly-protonated.

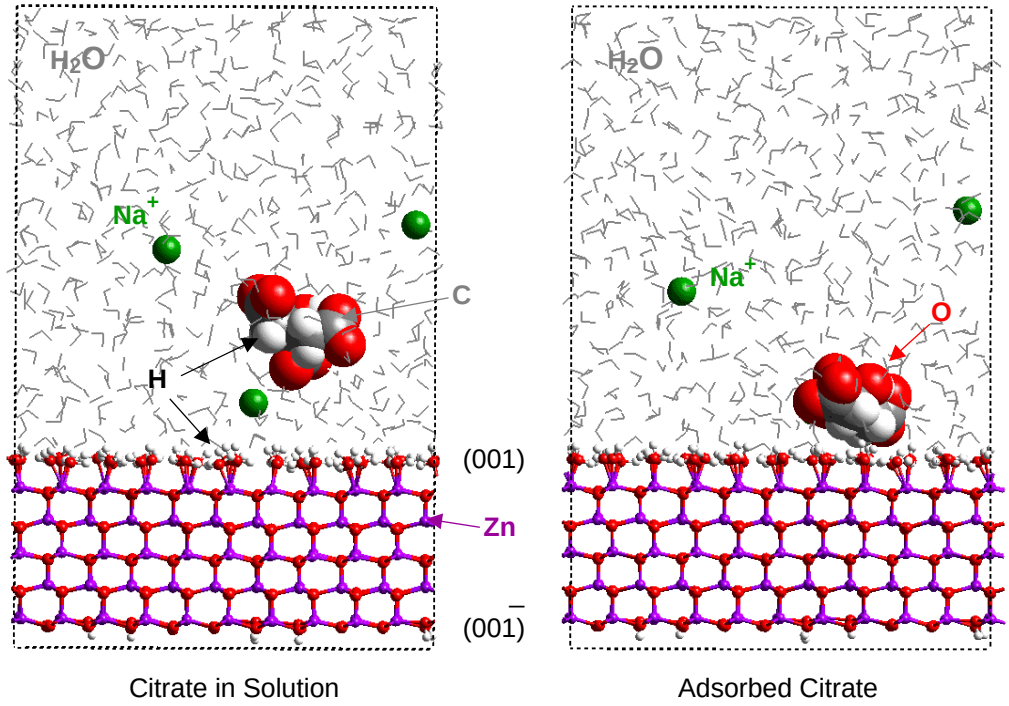

Figure 9. Diagrams of the full MD simulation cells for the (001) ZnO surface. The figure on the left represents a snapshot of the citrate anion in solution as it migrates toward the (001) surface. The figure on the right illustrates a snapshot of adsorbed citrate on the same surface. The third Na+ cation lies behind the citrate anion.

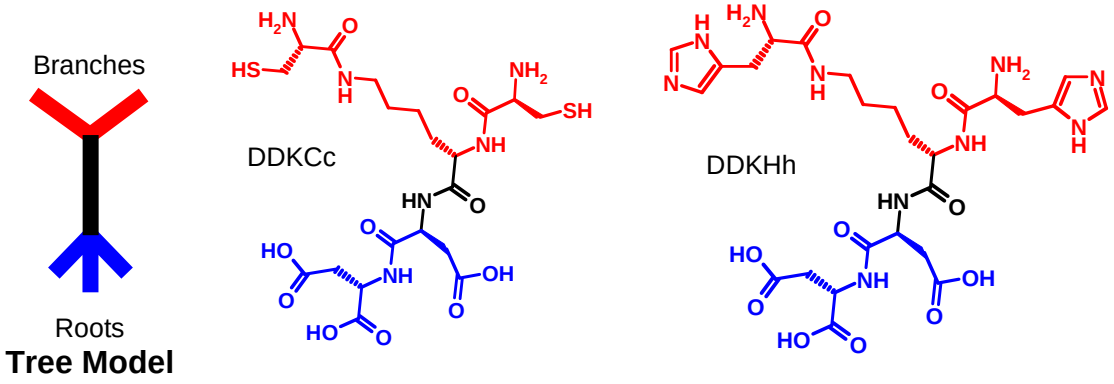

Figure 10. Schematic diagrams of peptide "tree model" and peptides synthesized based on this concept that have been shown to control the size of CdS nanocrystals.

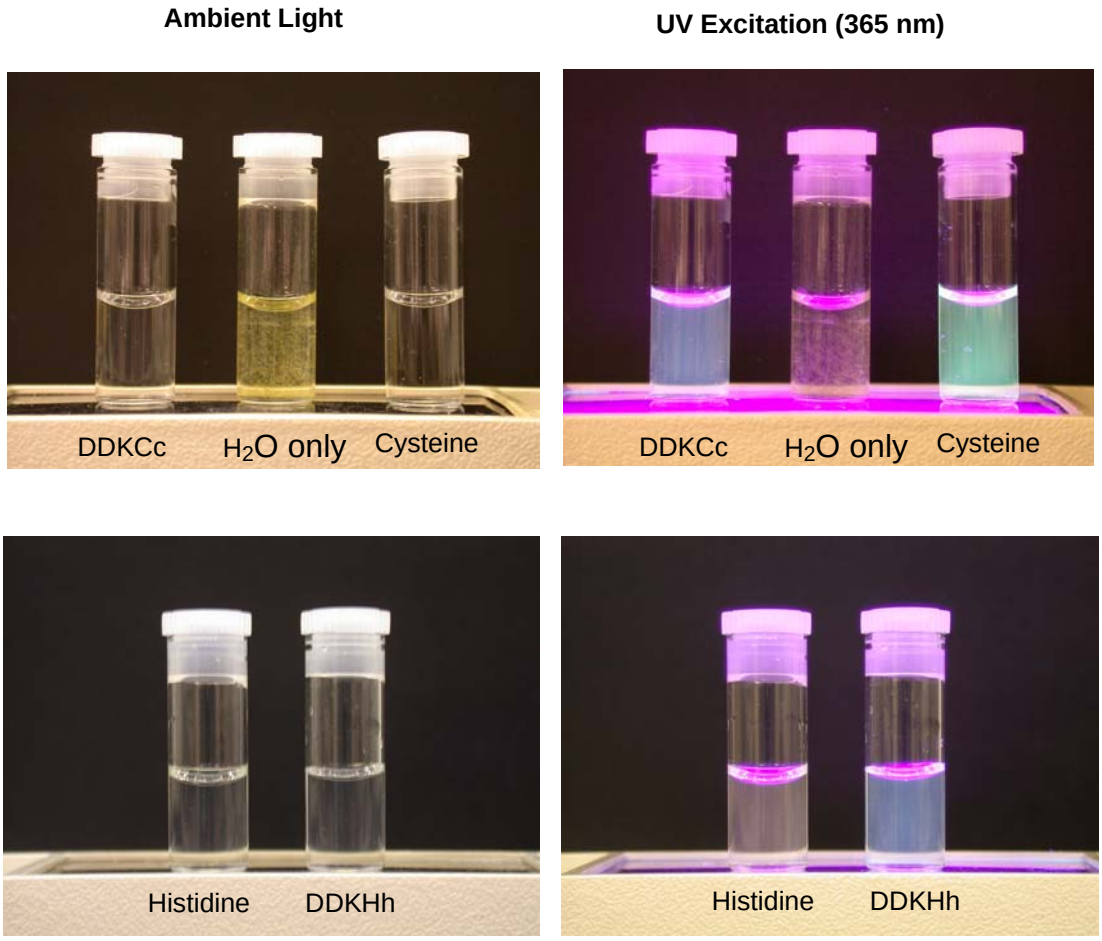

Figure 11. Examples of fluorescence of nanocrystals created using engineered dendritic peptides (Fig. 10).

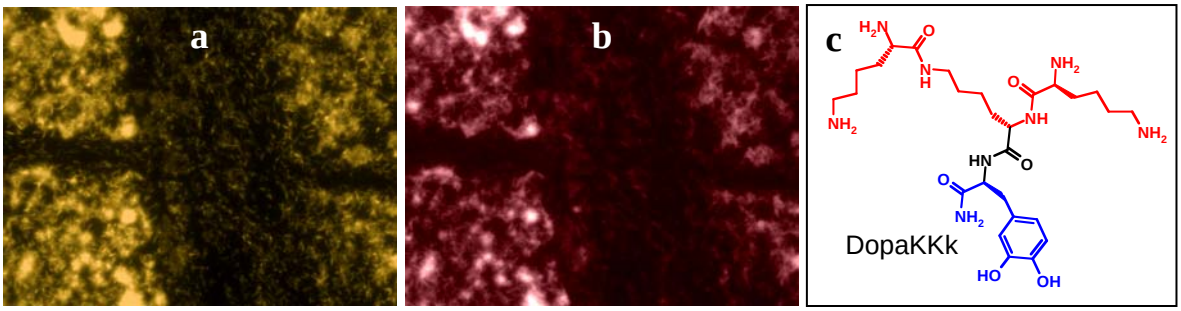

Figure12. Fluorescence images of: a) uncoated ZnO crystals and b) lysine-functionalized DOPA molecule (schematic – c) selectivity coated on the zinc oxide surfaces.

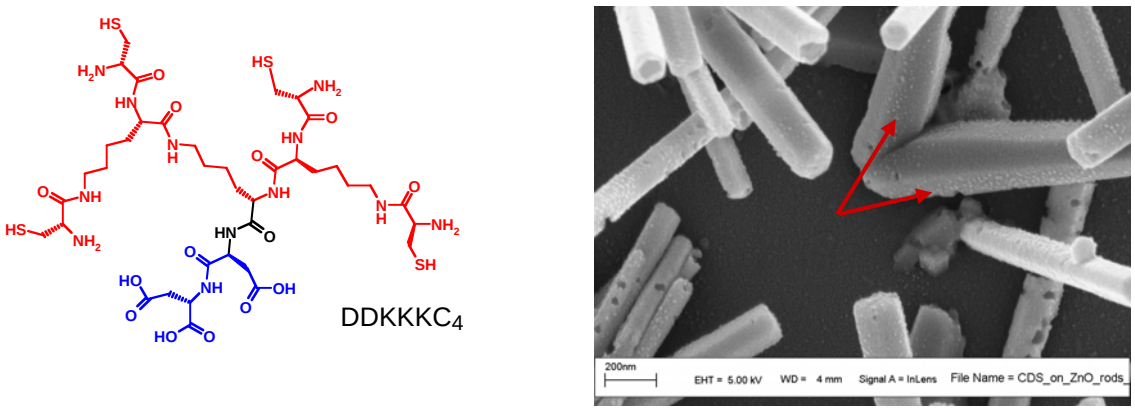

Figure 13. Cadmium sulfide nanocrystals (red arrows) grown on zinc oxide using a cysteine-containing DOPA peptide.

TABLES

Table 1. Site-types for Each ZnO Surface Studied Described by Coordination Number, Bond Length and Site Density

Surface	Surface Atom	Coordin. #	Zn-O Bond Lengths (Å)	Site Density (sites/nm^2)
100	O	1	1.973	5.92
100	O	3	1.973	5.92
			1.973	
			1.992	
001	O	1	1.992	10.9
$00\bar{1}$	O	3	1.973	10.9
			1.973	
			1.973	

Table 2. Protonation Reactions for ZnO Surface Sites Using the Revised MUSIC Model

	Log K
(100) Surface	
$pH_{zpc} = 8.68$	
$Zn-OH^{-0.494} + H^{+} \leftrightarrow Zn-OH_2^{+0.506}$	10.72
$Zn_3-O^{-0.506} + H^{+} \leftrightarrow Zn_3-OH^{+0.494}$	6.65
(001) Surface	
pH_{zpc} =11.23	
$Zn-OH^{-0.519} + H^{+} \leftrightarrow Zn-OH_2^{+0.418}$	11.26
(00 $\bar{1}$) Surface	
$pH_{zpc} = 6.13$	
$Zn_3-O^{-0.481} + H^{+} \leftrightarrow Zn_3-OH^{+0.519}$	6.13

Table 3. Average Potential Energies (kcal/mol) from Molecular Dynamics Simulations

	(001) ZnO Surface		**(100) ZnO Surface**	
Water Box	-3765			
ZnO + H_2O	-36179		-35625	
	3 Na^+ + 1 $Citrate^{3-}$	**1 Ethylene $Diamine^+$ + 1 Cl^-**	**3 Na^+ + 1 $Citrate^{3-}$**	**1 Ethylene $Diamine^+$ + 1 Cl^-**
Ions in Vacuum	NA*	NA	NA	NA
Ions in Water Box	-4450	NA	NA	NA
Solvation Energy	NA	NA	NA	NA
ZnO + Aq. Ions + H_2O	-36874	-36220	-36268	-35646
ZnO + Adsorbed Organic Ion + H_2O	-36880	-34501**	-36275	-35624
$\Delta E = E_{ads} - E_{aq}$	-6	1719**	-7	22

*NA – Not available.

**Ethylene diamine is not stable at (001) surface – these numbers represent the non-equilibrium energetics of the system when ethylene diamine is positioned at the surface.

REFERENCES

1. Li, W. Z. *et al.* Large-scale synthesis of aligned carbon nanotubes. *Science* **274**, 1701-1703 (1996).
2. Ren, Z. F. *et al.* Synthesis of large arrays of well-aligned carbon nanotubes on glass. *Science* **282**, 1105-1107 (1998).
3. Huang, M. H. *et al.* Room-temperature ultraviolet nanowire nanolasers. *Science* **292**, 1897-1899 (2001).
4. Wu, Y. *et al.* Inorganic semiconductor nanowires: rational growth, assembly, and novel properties. *Chem. Eur. J.* **8**, 1260-1268 (2002).
5. Huang, M. H. *et al.* Catalytic growth of zinc oxide nanowires by vapor transport. *Adv. Mater.* **13**, 113-116 (2001).
6. Lyu, S. C. *et al.* Catalytic growth of zinc oxide nanowires by vapor transport. *Chem. Phys. Lett.* **363**, 134-138 (2002).
7. Wu, J. J. & Liu, S. C. Low-temperature growth of well-aligned ZnO nanorods by chemical vapor deposition. *Adv. Mater.* **14**, 215-218 (2002).
8. Liu, S. C. & Wu, J. J., Low-temperature and catalyst-free synthesis of well-aligned ZnO nanorods on Si. *J. Mater. Chem.* **10**, 3125-3129 (2002).
9. Park, W. I., Kim, D. H., Jung, S. W. & Yi. S. C. Metalorganic vapor-phase epitaxial growth of vertically well-aligned ZnO nanowires. *Appl. Phy. Lett.* **80**, 4232-4234 (2002).
10. Lee, C. J. *et al.* Field emission from well-aligned zinc oxide nanowires grown at low temperature. *Appl. Phy. Lett*. **81**, 3648-3650 (2002).
11. Yu, D. P. *et al.* Controlled growth of oriented amorphous silicon nanowires via a solid-liquid-solid (SLS) mechanism. *Physica E* **9**, 305-309 (2001).
12. Chen, L. C. *et al.* Catalyst-free and controllable growth of SiC_xN_y nanorods. *J. Phys. Chem. Solids* **62**, 1567-1576 (2001).
13. Pan, Z. W., Dai, Z. R. & Wang, Z. L. Nanobelts of semiconducting oxides. *Science* **291**, 1947-1949 (2001).
14. Vayssieres, L., Keis, K., Hagfeldt, A. & Lingdquist, S. E. Three-dimensional array of highly oriented crystalline ZnO microtubes. *Chem. Mater*. **13**, 4395-4398 (2001).
15. Vayssieres, L., Keis, K., Lingdquist, S. E. & Hagfeldt, A. Purpose-built anisotropic metal oxide material: 3D highly oriented microrod array of ZnO. *J. Phys. Chem. B* **105**, 3350-3352 (2001).
16. Li, Y., Meng, G. W., Zhang, L. D. & Phillipp, F. Ordered semiconductor ZnO nanowire arrays and their photoluminescence properties. *Appl. Phys. Lett*. **76**, 2011-2013 (2000).
17. Li, Y., Cheng, G. S. & Zhang, L. D. Fabrication of highly ordered ZnO nanowire arrays in anodized alumina. *J. Mater. Res*. **15**, 2305-2308 (2000).
18. (a) Wang, Y. C., Leu, I. C. & Hon, M. H. Preparation of nanosized ZnO arrays by electrophoretic deposition. *Electrochemical Solid State Lett.* **5**, C53-C55 (2002). (b) Wang, Y. C., Leu, I. C. & Hon, M. H. Catalytic growth of semiconducting zinc oxide nanowires and their photoluminescence properties. *J. Cryst. Growth* **237**, 564-568 (2002).
19. For review, see Look, D. C. Recent Advances in ZnO materials and devices. *Mater. Sci. Engr. B* **80**, 383-387 (2001).

20. Huang, Y. Q., Liu, M. D., Zeng, Y. K. & Liu, S. B. Progress of study on ZnO thin films and its properties. *J. Inorg. Mater*. **16**, 391-397 (2001).
21. Kind, H., Yan, H., Messer, B., Law, M. & Yang, P. Nanowire ultraviolet photodetectors and optical switches. *Adv. Mater.* **14**, 158-160 (2002).
22. Wu, Y., Yan, H. & Yang, P. Semiconductor nanowire array: potential substrates for photocatalysis and photovoltaics. *Topics in Catalysis* **19**, 197-202 (2002).
23. Gordillo, G. New materials used as optical window in thin film solar cells. *Surf. Rev. Lett*. **9**, 1675-1680 (2002).
24. Lin, C. H., Chiou, B. S., Chang, C. H. & Lin, J. D. Preparation and cathodoluminescence of ZnO phosphor. *Mater. Chem. Phys*. **77**, 647-654 (2003).
25. Martin, P. M., Good, M. S., Johnston, J. W., Bond, L. J. & Crawford, S. L. Piezoelectric films for 100-MHz ultrasonic transducers. *Thin Solid Films* **379**, 253-258 (2000).
26. Muthukumar, S., Gorla, C. R., Emanetoglu, N. W., Liang, S. & Lu, Y. Control of morphology and orientation of ZnO thin films on SiO_2/Si substrates. *J. Cryst. Growth* **225**, 197-201 (2001).
27. Leviinson, L. M. & Philipp, H. R. Application and characterization of ZnO varistors. in *Ceramic Materials for Electronics* (ed. Buchanan, R. C. & Dekker, M.) 349-378 (New York, 1991).
28. Xu, J. Q., Pan, Q. Y., Shun, Y. A. & Tian, Z. Z. Grain size control and gas properties of ZnO gas sensors. *Sensors and Actuators B: Chem.* **66**, 277-279 (2000).
29. Pal. B. & Sharon, M., Enhanced photocatalytic activity of highly porous ZnO thin films prepared by sol-gel process. *Mater. Chem. Phys*. **76**, 82-87 (2002).
30. (a) Tian, Z. R., Voigt, J. A., Liu, J., Mckenzie, B. & Mcdermott, M. J., Biomimetic Arrays of Oriented Helical ZnO Nanorods and Columns. *J. Am. Chem. Soc*. **124**, 12954-1295 (2002). (b) Liu, J.; Lin, Y.; Liang, L.; Voigt, J. A.; Huber, D. L.; Tian, Z. R.; Coker, E.; Mckenzie, B.; Mcdermott, M. J. Templateless Assembly of Molecularly Aligned Conductive Polymer Nanowires: A New Approach for Oriented Nanostructures, *Chem. A Eur. J*., **9**, 604-611 (2003).
31. Jolivet, J. P., Gzara, M., Mazieres, J. & Lefebvre, J. Physicochemical study of aggregation in silver colloids. *J. Colloid Interface Sci.* **107**, 429-441 (1985).
32. López-Macipe, A., Gómez-Morales, J. & Rodríguez-Clemente, R. The role of pH in the adsorption of citrate on hydroxyapatite. *J. Colloid Interface Sci*. **200**, 114-120 (1998).
33. Hidber, P. C., Graule, T. J. & Gauckler, L. J. Citric acids: a dispersant for aqueous alumina suspensions. *J. Am. Ceram. Soc.* **79**, 1857-1867 (1996).
34. Biggs, S., Scales, P. J., Leong, Y. K. & Healy, T. W. Effects of citrate adsorption on the interactions between zirconia surfaces. *J. Chem. Soc.-Faraday Trans.* **91**, 2921-2928 (1995).
35. Liu, C. & Huang, P. M. Atomic force microscopy and surface characteristics of iron oxides fromed in citrate solutions. *Soil. Sci. Soc. Am. J*. **63**, 65-72 (1999).
36. Numerous papers have been published in this area. Some good references can be found in *Advanced in Crystal Growth Research* (ed. Sato, K,; Furukawa, Y.; Nakajima, K.) (Weizmann Inst. Sci., Israel, 2001)
37. Taubert, A., Glasser, G. & Palms, D. Kinetics and particle formation mechanism of zinc oxide in polymer-controlled precipitation from aqueous solution. *Langmuir* **18**, 4488-4494 (2002).

38. Taubert, A., Palms, D., Weiss, Ö., Piccini, M. T. & Batchelder, D. N. Polymer-assisted control of particle morphology and particle size of zinc oxide precipitated from aqueous solution. *Chem. Mater*. **14**, 2594-2601 (2002).
39. Jackson, A. P., Vincent, J. F. V. & Turner, R. M. The mechanical design of nacre. *Proc. Royal Soc. London B* **234**, 415-440 (1988).
40. Belcher, A. M. *et al.* Control of crystal phase switching and orientation by soluble mollusc-shell proteins. *Nature* **381**, 56-58 (1996).
41. Tian, Z. R.; Voigt, J. A., Liu, J.; Mckenzie, B.; Xu. H. Large Oriented Aarrays and Continuous Films of TiO2 Based Nanotubes, submitted to *J. Am. Chem. Soc*., 2003.
42. Demianets, L.N., and Kostomarov, D.V. Mechanism of Zinc Oxide Single Crystal Growth under Hydrothermal Conditions. Ann. Chim. Sci. Mat., 26, 193-198 2001.
43. Li, W.-J., Shi, E.-W., Zhong, W.-Z., and Yin, Z.-W. Growth mechanism and growth habit of oxide crystals. Journal of Crystal Growth, 203, 186-196, 1999.
44. Sabine, T. M. and Hogg, S. Wurtzite Z Parameter for Beryllium Oxide and Zinc Oxide. Acta Crystallographica Section B- Structural Crystallography and Crystal Chemistry, B25, 2254-2256, 1969.
45. Hiemstra, T., and van Riemsdijk, W.H. A Surface Structural Approach to Ion Adsorption: The Charge Distribution (CD) Model. Journal of Colloid and Interface Science, 179, 488-508, 1996.
46. Venema, P., Hiemstra, T., and van Riemsdijk, W. H. Multisite Adsorption of Cadmium on Goethite. Journal of Colloid and Interface Sciences, 183, 515-527, 1996.
47. Hiemstra, T., Venema, P., and van Riemsdijk, W.H. Intrinsic Proton Affinity of Reactive Surface Groups of Metal (Hydr)oxides: The Bond Valence Principle. Journal of Colloid and Interface Science, 184, 680-692, 1996.
48. Rappé, A.K., and Goddard, W.A.I. Charge equilibration for molecular dynamics simulations. Journal of Physical Chemistry, 3558-3363, 1991.
49. Dauber-Osguthorpe, P., Roberts, V.A., Osguthorpe, D.J., Wolff, J., Genest, M., and Hagler, A.T. Structure and Energetics of Ligand Binding to Proteins: *Esherichia coli* Dihydrofolate Reductase-Trimethoprim, A Drug-Receptor System. PROTEINS: Structure, Function, and Genetics, 4, 31-47, 1988.
50. Rappé, A.K., Casewit, C.J., Colwell, K.S., Goddard, W.A.I., and Skiff, W.M. UFF, a full periodic table force field for molecular mechanics and molecular dynamics simulations. Journal of American Chemical Society, 114, 10024-10035, 1992.
51. Harris, F.E. Ewald Summations in Systems with Two-Dimensional Periodicity. International Journal of Quantum Chemistry, 68, 385-404, 1998.
52. Karasawa, N., and Goddard, W.A.I. Acceleration of Convergence for Lattice Sums. Journal of Physical Chemistry, 93, 7320-7327, 1989.

Distribution:

1	MS 0123	H.R. Westrich, 1011
1	MS 0887	M.J. Cieslak, 1800
1	MS 0885	D.B. Dimos, 1803
1	MS 0886	B.B. McKenzie, 1822
1	MS 1411	J. Liu, 1846
1	MS 1411	D.L. Moore, 1846
1	MS 1411	E.D. Spoerke, 1846
5	MS 1411	J.A. Voigt, 1846
1	MS 0750	L.J. Criscenti, 6118
1	MS 0750	R.T. Cygan, 6118
1	MS 9018	Central Technical Files, 8945-1
2	MS 0899	Technical Library, 9616